www.springer.com/41230
https://doi.org/10.1007/s41230-025-4031-3
Research & Development Vol. 22 No. 3 May 2025 CHINA FOUNDRY

# Quantitative analysis of columnar-to-equiaxed transition in Mg-Gd-Zn alloys

***Yong-biao Wang[1], Bao-qi Ma[1], Jia-xin Wang[1], **Xin-tian Liu[1], Ang Zhang[2], Jian-xiu Liu[1], Yan Wang[2], Yu-juan Wu[3], and Li-ming Peng[3]**

*1. Henan Key Laboratory of Intelligent Manufacturing of Mechanical Equipment, Zhengzhou University of Light Industry, Zhengzhou 450002, China*

*2. National Engineering Research Center for Magnesium Alloys, College of Materials Science and Engineering, Chongqing University, Chongqing 400044, China*

*3. National Engineering Research Center of Light Alloy Net Forming and State Key Laboratory of Metal Matrix Composite, Shanghai Jiao Tong University, Shanghai 200240, China*

**Abstract:** Columnar to equiaxial crystal transition (CET) is an important technological feature in many casting processes. This work investigated the CET during the solidification of Mg-Gd-Zn alloys by combining synchrotron radiation in-situ imaging and phase-field method. Results show that the grain size, dendrite tip radius, and secondary dendrite arm spacing (SDAS) all exponentially decrease with an increase in cooling rate ($V_c$). The variation in the radius of the dendritic tip is similar to the prediction of the Hunt model, while the variation in the SDAS is close to the Bouchard-Kirkaldy model. It is worth noting that the CET is promoted by a decrease in the temperature gradient ($G$) and an increase in the cooling rate ($V_c$). In both equiaxed and columnar crystal regions, the dendrite tip growth rate and solid phase volume fraction increase with increasing $G$ and $V_c$. In addition, the CET process has been predicted by simulation. The results are consistent with the predictions of the GTK model, which is important for the in-depth study of the dendrite morphology in different crystallization regions. In the final stage, the effects of different critical subcooling degrees and nucleation densities on the CET were explored. The results show that increasing the critical nucleation supercooling degree can inhibit the generation of equiaxial crystals, while increasing the nucleation density helps to promote the CET.

**Keywords:** Mg-Gd-Zn alloys; solidification; synchrotron radiation in-situ imaging; phase-field method; equiaxial crystal transition

**CLC numbers:** TG146.22 **Document code:** A **Article ID:** 1672-6421(2025)03-239-13

## 1 Introduction

With the growing demand for lightweight materials across various fields, magnesium alloys, called 'green engineering materials in the 21st century', are seeing wider applications due to their low density, high specific strength and stiffness, excellent electromagnetic shielding performance, and outstanding vibration damping capacity[1-2]. The rare-earth elements, such as Gd, Y, Ce, and Nd, can further improve the strength and plastic processing capacity of the magnesium alloys.

Recently, Mg-Gd-Zn alloys with a close-packed hexagonal structure have been widely used in aerospace and defense applications due to their high specific strength and excellent plasticity[3-4]. However, poor corrosion resistance and low heat resistance limit the further application of Mg-Gd-Zn alloys. The microstructures formed during the solidification play an important role in determining the final properties of alloys. So, predicting and controlling the formation of solidification microstructures becomes a key to optimizing the alloy properties. There are two main solidification microstructures including columnar and equiaxed crystal structures. The columnar crystal structure imparts directional properties to castings, whereas the equiaxed crystal structure results in more isotropic

***Yong-biao Wang**

Male, born in 1984, Ph. D., Professor. His research interest mainly focuses on the simulation of the microstructure of lightweight alloys.

E-mail: wsbiaoyongwang@163.com

****Xin-tian Liu**

E-mail: liuxintian224@163.com

**Received: 2024-02-17; Revised: 2024-05-06; Accepted: 2024-07-10**

and uniform material properties[5-10]. Therefore, studying the columnar-to-equiaxed transition (CET) mechanism in magnesium alloys is of great significance to improve the alloy properties and expand the application of the magnesium alloys.

Over the past decades, extensive studies have been conducted to investigate the CET phenomenon in alloys. Hunt et al.[11] proposed that equiaxial crystals can appear along the columnar crystal front during the directional solidification and predicted the time when all grains can be transformed into equiaxial crystals. Sturz et al.[12] found that the length of the columnar crystal region decreased with the increase of cooling rate in the CET experiments. Zaïdat et al.[13] found that the CET phenomenon became more obvious with the increase of the pulling speed when the temperature gradient was constant. Gäumann et al.[14-15] studied the effects of nucleation undercooling and solute content on the grain structure transition. The nucleation undercooling along the front of the columnar grain boundary was the main factor causing the CET phenomenon. However, above experiments lack real-time observation of the CET phenomenon, and the solidification information might be incomplete. The development of synchrotron radiation technology compensates for the previous limitations in real-time observation of solidification microstructures. Mathiesen et al.[16] observed similar results to those reported by Gäumann et al.[15] using the synchrotron radiation technology. Kang et al.[17] found that the CET of the Al-20wt.%Cu alloy was caused by fragmentation behavior and nucleated dendrites. Recently, Garces et al.[18] studied the effect of temperature on the load partitioning evolution of Ti particles reinforced magnesium metal matrix composite by in-situ synchrotron radiation. Xin et al.[19] revealed the complete sequence of phase transformations in the alloy and provided morphological evidence for the transformation mechanisms.

With the rapid development of numerical methods, the phase-field simulation has been widely used to study the CET. Badillo et al.[20] used the phase-field method to quantitatively study the effects of temperature gradient, solidification rate, nucleation spacing, nucleation undercooling, and anisotropic strength on the CET of the Al-3wt.% Cu alloy. Li et al.[21] adopted the phase-field method to study the effects of cooling rate on the CET and found that both the length of columnar crystals and the size of equiaxed crystals increased with the decrease of cooling rate. Viardin et al.[22] found that excessive nucleation undercooling inhibited the formation of equiaxed crystals at the interface front. Rátkai et al.[23] obtained results similar to Hunt's model[11] by analyzing temperature gradient and solidification rate effects on the CET in Ag-Cu alloys. Lenart et al.[24] predicted the range of CET under different temperature gradients and solidification rates. Montiel et al.[25] quantitatively predicted the effects of nucleating agent on the CET phenomenon, and found that the length of columnar crystal region increased with the increase of nucleation factor, which was roughly the same as the GTK theory[14]. Raghavan et al.[26] studied the effect of heat transfer in electron beam additive manufacturing on the grain morphology of IN718 and manipulated the relative number of voxels that lie in the columnar or equiaxed region. Later, Nabavizadeh et al.[27] studied the CET during the directional solidification of Inconel 718 alloy, found that while the initial grain size did not affect the average grain size of equiaxed growth, it significantly affected the primary dendrite arm spacing (PDAS) of columnar growth.

Although these studies obtained good results, most of them have focused on materials with a cubic crystal structure, and systematic investigations into the CET in hexagonal systems remain rare. Wang et al.[28] revealed the effects of cooling rate on the CET of Mg-6wt.%Gd alloy, and they found that the CET phenomenon was obvious when the cooling rate was in the range of 0.5–1 $K\cdot s^{-1}$, which provided a foundation for further exploration on the CET mechanism. The dendrites morphology under cubic or hexagonal systems were different and the conditions of the CET were also not exactly the same. Therefore, further study on CET is necessary.

In this work, the CET process of the Mg-15Gd-Zn (wt.%) alloy was quantitatively studied by combining synchrotron radiation in-situ imaging technology and phase-field simulation. The results in this work were compared with other theoretical models. The effects of cooling rate and temperature gradient on dendrite growth in different crystal regions were analyzed by using a phase field model, and each crystal transition region was predicted. Finally, the results obtained by investigating the effects of critical nucleation supercooling and nucleation density on the CET provide useful guidance for deepening the theoretical understanding of the CET in other magnesium alloys. These research results not only help to optimize the mechanical properties of the materials, but also provide useful information to promote the development and wide application of magnesium alloys.

## 2 Experimental method

The synchrotron radiation experiments were carried out in Shanghai Light Source BL13W1 station. The raw materials were pure Mg (purity 99.9wt.%), pure Zn (purity 99.9wt.%), and Mg-25Gd (wt.%). The ingot was cut, ground, and polished to prepare rectangular samples with the a length of 7 mm, a width of 6 mm, and a height of 0.5 mm. Then, the samples were put into a graphite sheet on the 0.12 mm thick $Al_2O_3$ ceramics. Finally, the samples were sealed by high-temperature binder between two $Al_2O_3$ ceramics. The sample sealing diagram is shown in Fig. 1(a). The heating furnace and the cooling system are shown in Fig. 1(b). First, the interior of the furnace was evacuated to a vacuum and filled with high-purity argon, an inert gas, to prevent the sample from oxidizing during the heating process. Then, the temperature was raised to 883 K for 5–10 min until the sample melted, and finally cooled down at 1.5 $K\cdot min^{-1}$. Inside the furnace, two separate heating zones were configured, upper and lower, which can be independently operated to create temperature gradient. In addition, internal thermocouple sensors can provide instant temperature feedback from each zone. A temperature logging system connected to a computer records and stores the temperature data from the thermocouple sensors in real time. When the X-ray penetrates the sample, the charge coupled device (CCD) detector, capable of high-speed reading and writing, receives the X-ray with phase information to finish dynamic imaging. The X-ray energy was set to 20 keV, the image capture interval was 0.5 s, and the distance from the heating furnace to the CCD detector was kept at 0.5 m to ensure the acquisition of high-resolution images. The specific operating principle and process parameters were described in Refs. [29, 30]. The secondary dendrite arm spacing (SDAS) was directly measured by the Image Pro Plus.

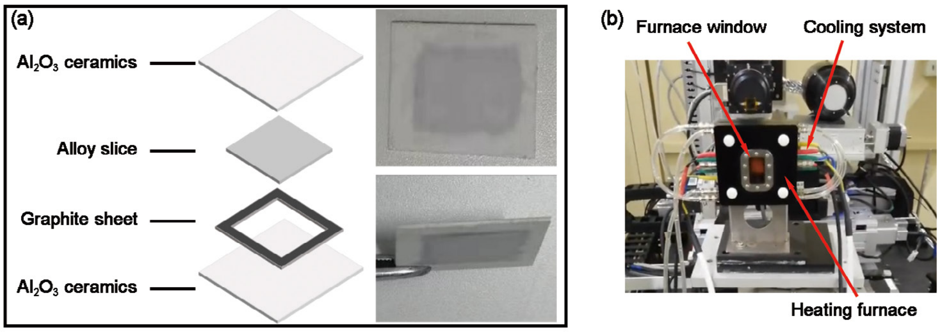

Fig. 1: Schematic of Mg-15Gd-Zn (wt.%) sample (a) and vacuum furnace (b)

# 3 Phase-field model

Based on the phase-field model in Ref. [31], a two-dimensional solidification model with random nucleation was established for the Mg-15Gd-Zn (wt.%) alloy. The frozen temperature approximation was used to determine the temperature distribution:

$$T(y)=T_0+G(y-V_\mathrm{p}t) \tag{1}$$

where $G$ is the temperature gradient in the $y$ direction, $T_0$ is the initial temperature at the bottom of the simulated region, and $V_\mathrm{p}$ is the solidification rate, which is defined as the ratio of the cooling rate ($V_\mathrm{c}$) to the temperature gradient ($G$). The dimensionless temperature is expressed as follows:

$$\tilde{T}=\frac{y-V_\mathrm{p}t}{l_\mathrm{T}} \tag{2}$$

where $l_\mathrm{T}=|m|(1-k)c_0/(kG)$, $k$ is the solute partition coefficient and $c_0$ is the initial liquid concentration.

The order parameter $\varphi(r, t)$ continuously changes from $-1$ in the liquid phase to 1 in the solid phase. The concentration field $c(r, t)$ is represented by a supersaturated field $U=\{(2kc/c_0)/[1+k-(1-k)h(\varphi_i)]-1\}/(1-k)$, where $h(\varphi_i)=-1+\sum_i(\varphi_i+1)$ is an interpolation function varying from $-1$ to 1[31]. To describe the dendrite morphology more realistically, the anisotropy function was introduced. For magnesium alloys with a close-packed hexagonal structure, the equation is expressed as[32]:

$$a_\mathrm{s}(\phi-\phi_0)=1+\varepsilon\cos\left[6(\phi-\phi_0)\right] \tag{3}$$

where $\phi$ is the angle between the interface normal and the $y$ direction, $a_\mathrm{s}$ is the anisotropic function, $\varepsilon$ is the anisotropic strength and $\phi_0$ is the angle between the dendrite preferred growth direction and heat flow direction.

The governing equation of the phase field and supersaturated field is as follows [31]:

$$\begin{aligned}\tau_0 a_\mathrm{s}^2(\phi-\phi_0)\left[1-(1-k)\tilde{T}\right]\frac{\partial\varphi_i}{\partial t}&=W_0^2\nabla\left[a_\mathrm{s}^2(\phi-\phi_0)\nabla\varphi_i\right]\\&+\varphi_i-\varphi_i^3+W_0^2\sum\nolimits_{m=x,y}\left[\partial_m\left(\left|\nabla\varphi_i\right|^2 a_\mathrm{s}(\phi-\phi_0)\frac{\partial a_\mathrm{s}(\phi-\phi_0)}{\partial(\partial_m\varphi_i)}\right)\right]\\&-\lambda\left(1-\varphi_i^2\right)^2\left(U+\tilde{T}\right)-a\left(\frac{1+\varphi_i}{2}\right)\sum\nolimits_{j\neq i}\left(\frac{1+\varphi_j}{2}\right)^2\end{aligned} \tag{4}$$

$$\begin{aligned}\frac{\left[1+k-(1-k)h(\varphi_i)\right]}{2}\frac{\partial u}{\partial t}&=\nabla\left\{D_1\frac{1-h(\varphi_i)}{2}\nabla U-\vec{j}_\mathrm{AT}\right\}\\&+\frac{1}{2}\left[1+(1-k_i)U\right]\sum\nolimits_i\frac{\partial\varphi_i}{\partial t}\end{aligned} \tag{5}$$

where $\tau_0=a_2\lambda W_0^2/D_1$ is the relaxation time, $W_0=d_0\lambda/a_1$ is the interface thickness, $d_0$ is the capillary length, $\lambda$ is the phase field coupling coefficient, $a_1$=0.8839, $a_2$=0.6267. $\vec{j}_\mathrm{AT}$ is the antitrapping current, which maintains the local equilibrium of the solid-liquid interface by eliminating unphysical interface effects:

$$\vec{j}_\mathrm{AT}=-\frac{1}{2\sqrt{2}}W_0 a_\mathrm{s}(\phi-\phi_0)\left[1+(1-k_i)U\right]\sum\nolimits_i\partial t\,\varphi_i\frac{\nabla\varphi_i}{\left|\nabla\varphi_i\right|} \tag{6}$$

The heterogeneous nucleation model[33] is introduced to reproduce the CET process. The number of nuclei formed in each time step was calculated as follows:

$$\frac{\partial N_1}{\partial t}=-2\mu_\mathrm{n}\Delta TV_\mathrm{c}(1-f_\mathrm{s}) \tag{7}$$

where $\mu_\mathrm{n}$ is a nucleation parameter related to nucleation density $N_0$, $\Delta T$ is the degree of undercooling, $f_\mathrm{s}$ is the volume fraction of the solid phase.

The probability of nucleation in liquid is defined as:

$$P=\frac{\partial N_1}{N_0^1} \tag{8}$$

where $N_0^1$ is the number of unsolidified nodes. When the nucleation probability $P$ is greater than a random number between 0 and 1, nucleation randomly occurs. The physical parameters of the Mg-15Gd-Zn (wt.%) alloy are listed in Table 1[34-36].

Table 1: Material parameters that define Mg-15Gd-Zn (wt.%) alloy[34-36]

| Parameter | Symbol | Value | Unit |
|---|---|---|---|
| Liquidus slope | $m$ | 3.0 | $\text{K}\cdot(\text{wt.\%})^{-1}$ |
| Initial solute concentration | $C_0$ | 15.0 | wt.% |
| Solute partition coefficient | $k$ | 0.35 | |
| Temperature gradient | $G$ | 1–100 | $\text{K}\cdot\text{mm}^{-1}$ |
| Solutal diffusion coefficient | $D_\text{l}$ | 1,400 | $\mu\text{m}^2\cdot\text{s}^{-1}$ |
| Gibbs-Thomson coefficient | $\Gamma$ | 0.37 | K·μm |
| Melting point of Mg | $T_\text{M}$ | 883 | K |
| Two-phase situation | $\Delta H$ | 2.35 | $\text{J}\cdot\text{kg}^{-1}$ |
| Latent heat of fusion | $L$ | 610 | $\text{J}\cdot\text{cm}^{-3}$ |
| Space step size | d$x$ | 0.8 | |
| Time step size | d$t$ | 0.025 | |

# 4 Results and discussion

## 4.1 Comparison between experimental and simulated results

Figure 2 shows the synchrotron imaging results and the phase field simulation results of dendrite evolution in the Mg-15Gd-Zn (wt.%) alloy under different cooling rates, with the $G$ maintained at 4 $\text{K}\cdot\text{mm}^{-1}$. As shown in the Fig. 2, the α-Mg dendrite appears as a bright grain structure, and the simulation results are in agreement with the experimental observations. The grains start to nucleate on the inner wall of the casting as the initial nucleation point. When $V_\text{c}$ is low, e.g., 0.025 $\text{K}\cdot\text{s}^{-1}$ in Figs. 2(a1–a4), a small number of initial grains nucleate, but a great number of secondary and tertiary dendrite arms are generated from the developed primary trunks. As the solidification proceeds, significant CET can be observed in the front of the columnar crystals, and a number of ellipsoidal equiaxed crystals form, as circled by the red ellipses in Fig. 2(a2). Figures 2(b1–b4) and (c1–c4) show the dendrite growth process with $V_\text{c}$ of 0.05 $\text{K}\cdot\text{s}^{-1}$ and 0.1 $\text{K}\cdot\text{s}^{-1}$, respectively. In comparison with Figs. 2(a1–a4), the dendrite size becomes smaller, but the number of grains increases. When $V_\text{c}$ reaches 0.25 $\text{K}\cdot\text{s}^{-1}$, the driving force for nucleation increases, and the grains are easier to nucleate. The nucleated grains are also clearly observed in the liquid phase at early solidification stage, as shown in Figs. 2(d1–d4). The increase of the nucleation density inhibits the secondary dendrite arms and makes the dendrites smaller. Moreover, some dendrites nucleating at later solidification stage are blocked by the surrounding mature dendrites, making them enter the coarsening stage once they nucleate. The growth of columnar crystals is completely inhibited, and all dendrites exist in the form of equiaxed crystals. Accordingly, increasing the cooling rate is not only conducive to grain refinement but also beneficial to inhibiting the growth of columnar crystals.

The grain size directly determines the mechanical properties of the alloys. Eskin et al.[37] conducted a series of casting tests regarding Al-Cu alloys under different cooling rates, cooling conditions, and copper concentrations. They found the relationship between the average grain size ($D$) and $V_\text{c}$ is: $D = AV_\text{c}^{n}$, where $A$ is a constant[33, 38], and $n$ is a growth factor, ranging between 0.2 and 0.5. When $n$ approaches 0.5, the effect is optimal. A statistical analysis of the dendrite size distribution was conducted. As shown in Fig. 3, the grain size in the simulation is slightly larger than that in the experiment, but they follow the same trend, that is the grain size gradually decreases and then being stabilized with the increase of the cooling rate. This is because a slower cooling rate results in a lower degree of subcooling, which in turn reduces the number of nucleation sites. Consequently, the dendrites can fully develop and grow to larger sizes. The simulation data are fitted as $D = 52.247V_\text{c}^{-0.475}$, with $n$=0.475, which is very close to 0.5.

By controlling the radius of the dendrite tip, the morphology and size of the crystal can be altered, thereby improving the scientific performance of the material. There are currently a large number of experimental results and theoretical models available for studying the radius of dendritic tips, among which the representative models are the Hunt model[11], the Kurz model[39], and the Trivedi model[40].

The mathematical expression of the Hunt model[11] is as follows:

$$R = \left[\frac{2\gamma D}{m(1-k)c_0 v}\right]^{0.5} \tag{9}$$

where $\gamma$ represents the Gibbs Thompson parameter.

Kurz et al. [39] found that there is a relationship between the dendrite tip radius $R$ and the dendrite growth speed $v$:

$$R = 2\pi\left[\frac{\gamma D}{m(1-k)c_0 v}\right]^{0.5} \tag{10}$$

The model proposed by Trivedi et al. [40] is shown as follows:

$$R = \left[\frac{2k\gamma D L_\text{l}}{m(1-k)c_0 v}\right]^{0.5} \tag{11}$$

In order to compare the differences of dendrite tip radius with the above models, the radius of the dendrite tip under different cooling rates was systematically analyzed, and the results are shown in Fig. 4. The predictions of different methods are not the same, but they have the same rule of change, which is that the radius of the dendrite tip decreases with the increase of $V_\text{c}$. When $V_\text{c}$ is low, the degree of subcooling decreases, which in turn leads to slow growth of dendrites. In this case, the diffusive expulsion of the solute is not sufficient, resulting in larger dendrite tips. With the increase of $V_\text{c}$, the growth rate accelerates and the amount of the discharged solute increases, reducing the dendrite tip radius. By observing the experimental and simulated results, it is found that both of them exhibit a similar

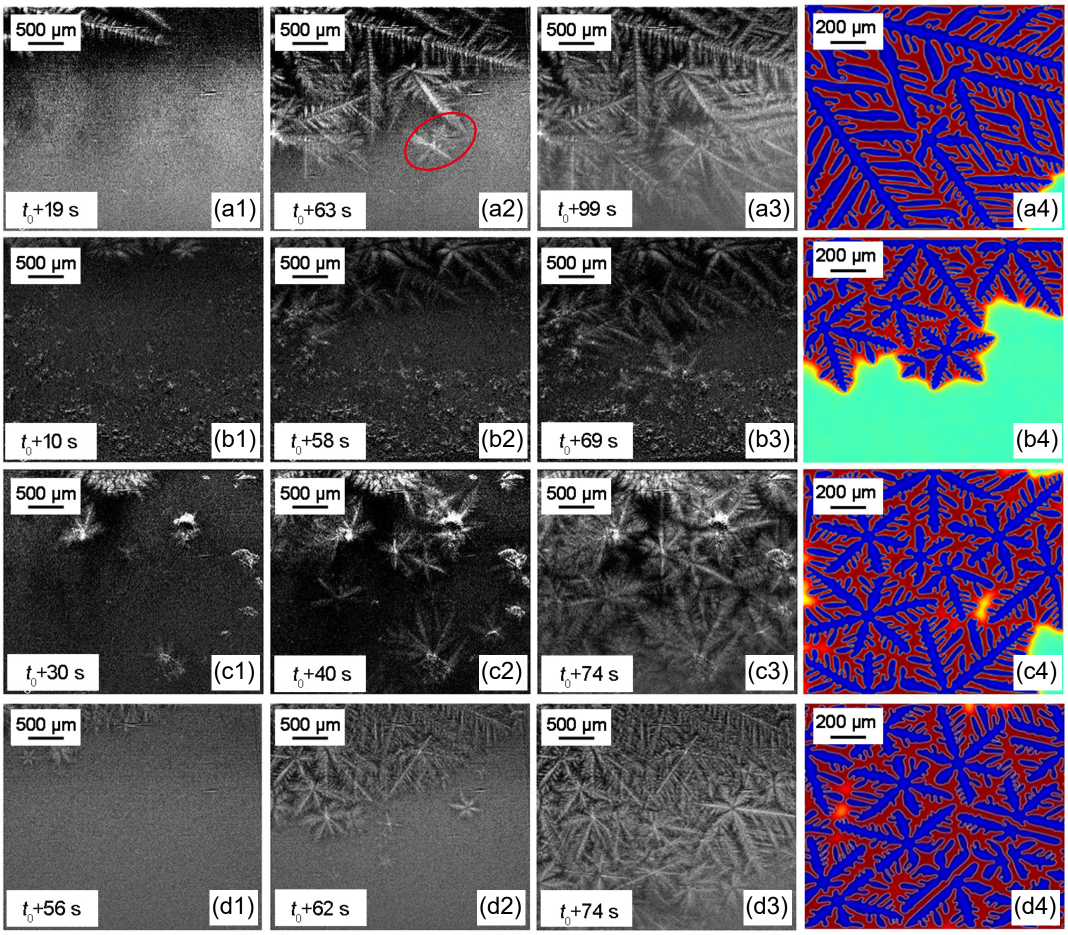

**Fig. 2: Evolution of dendrites in Mg-15Gd-Zn (wt.%) alloy at different cooling rates when $t_0$=30 s: (a1–a4) 0.025 K·s$^{-1}$; (b1–b4) 0.05 K·s$^{-1}$; (c1–c4) 0.1 K·s$^{-1}$; (d1–d4) 0.25 K·s$^{-1}$**

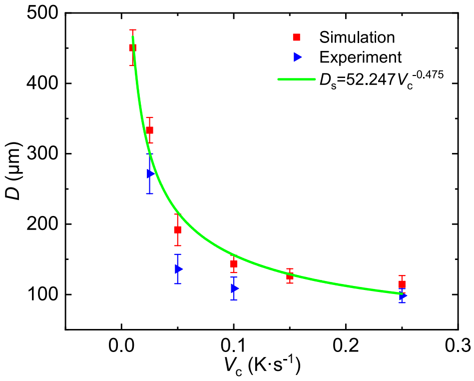

**Fig. 3: Variation curve of grain size (*D*) with cooling rate ($V_c$)**

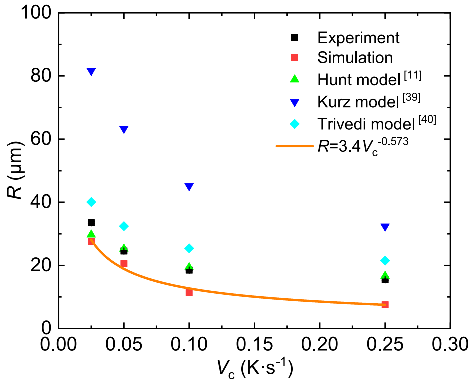

**Fig. 4: Variation of dendrite tip radius (*R*) with cooling rate ($V_c$) using different models**

trend of variation to the Hunt, Kurz, and Trivedi models. Further comparative analysis reveals that the simulated results are more closely aligned with the Hunt model, but far from the Kurz model. This is due to the fact that the Hunt model uses a more accurate numerical integration of the heat flow equations compared to the Kurz model. Combining the Hunt, Kurz, and Trivedi model with the trends in Fig. 4, the mathematical relation of the dendrite tip radius ($R$) changing with $V_c$ can be expressed as the power function $R = aV^{-b}$, where $a$ and $b$ are constants. The expression of the function obtained by fitting the simulated and experimental results is $R$=3.4$V_c^{-0.573}$.

Bouchard et al.[41] established the Bouchard-Kirkaldy model (BK theoretical model), which not only develops the theoretical analysis of dendrite growth mechanisms from the Trivedi-Somboonsuk model[42] (TS theoretical model) but also incorporates the concept from the Kattamis-Flemings model[43] (KF theoretical model) that solute redistribution influences solidification microstructures, thereby enabling effective prediction of the primary dendrite and SDAS ($\lambda_2$) of binary alloys.

The mathematical expression of the BK theoretical model is:

$$\lambda_2 = 2a_2\pi\left[\frac{4\sigma}{c_0(1-k)\Delta H}\left(\frac{D}{v}\right)^2\right]^{1/3} \tag{12}$$

where $a_2$ is the correction factor, $\sigma$ is the interface energy, $k$ is the solute partition coefficient, $\Delta H$ is the heat of fusion, and $D$

is the solute diffusion coefficient.

The functional form of the TS model is:

$$\lambda_2 = \left[\frac{8\gamma DL}{kv\Delta T_0}\right]^{0.5} \tag{13}$$

where $\Delta T_0 = m(k-1)c_0/k$ is the solidification temperature range, $v = GD/k\Delta T_0$ represents the growth rate, $L$ is a constant that depends on the harmonic of perturbation.

The analytical expression of the KF model is:

$$\lambda_2 = 5.5\left(Mt_{\mathrm{f}}\right)^{1/3} \tag{14}$$

$$M = \frac{\gamma D \ln\left(c_1^{\mathrm{m}}/c_0\right)}{m(1-k)\left(c_1^{\mathrm{m}}/c_0\right)} \tag{15}$$

where $t_{\mathrm{f}}$=$\Delta T/Gv$ is the solidification time, $M$ is the coarsening coefficient, and $c_1^{\mathrm{m}}$ is the maximum liquid phase concentration.

Both predicted and experimental SDAS results for the Mg-15Gd-Zn (wt.%) alloy at different cooling rates are shown in Fig. 5. When $V_{\mathrm{c}}$ is low, the predicted SDAS result by the BK theoretical model reaches 78 μm, while that of the KF model is 46 μm. As $V_{\mathrm{c}}$ increases to 0.25 K·s$^{-1}$, the experimental SDAS decreases to 43 μm, and the prediction value of the TS model is 12 μm. The SDAS changes exponentially with an increase in $V_{\mathrm{c}}$, although the predicted results vary with the adopted models. When $V_{\mathrm{c}}$ is low, the SDAS is large. With the increase of $V_{\mathrm{c}}$, the SDAS decreases rapidly and then becomes stable. This is because as $V_{\mathrm{c}}$ increases, the number of nucleation increases, the grain size decreases, and the SDAS are continuously refined. By comparison with the BK theoretical model, TS model, and the KF model, it can be observed the phase-field simulation is closer to that predicted by the BK theoretical model, but has a certain gap with those by the TS and KF models until $V_{\mathrm{c}}$=0.1 K·s$^{-1}$. When $V_{\mathrm{c}}$ comes to 0.25 K·s$^{-1}$, the dendrite arm spacing of the hexagonal system is more compact than the cubic system, and the results of the simulation are larger than the other models. Combining the BK, TS, and KF models with the trends in Fig. 5, the relationship between the simulated SDAS and $V_{\mathrm{c}}$ can be represented as a power function, i.e., $\lambda_2$=$aV_{\mathrm{c}}^{-b}$, where $a$ and $b$ are constants. Fitting the simulations and experiments yields the SDAS as a function of $V_{\mathrm{c}}$ as $\lambda_2$=20.49$V_{\mathrm{c}}^{-0.315}$.

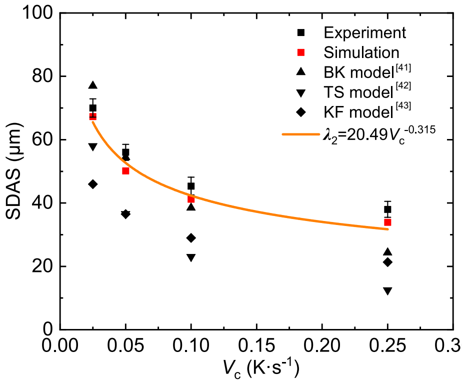

Fig. 5: Variation of SDAS with cooling rate using different models

## 4.2 Phase field simulation results for different solidification parameters

As the temperature gradient $G$ and cooling rate $V_{\mathrm{c}}$ vary, the dendritic morphology undergoes significant changes. Figure 6 shows the simulation results of the dendrite morphologies under different solidification conditions, in which the $x$-axis represents $G$, and the $y$-axis represents $V_{\mathrm{c}}$. The simulation area is 600$d_0$×1,500$d_0$, the dimensionless diffusion coefficient is 3.0 and other dimensionless parameters are as follows: $\tau_0$=1, $W_0$=4, $\lambda$=4, $\varepsilon$=0.05, the space step d$x$=d$y$=0.8, and the time step d$t$=0.025.

In the $x$-axis direction, the dendrite morphology is columnar crystals at a large temperature gradient. With an decrease in temperature gradient, the dendrite morphology changes and the CET region becomes apparent. The number of equiaxed crystals increases, eventually becoming the dominant structure. In the $y$-axis direction, the increase of $V_{\mathrm{c}}$ is conducive to the occurrence of the CET phenomenon, which makes the number of equiaxed crystals increase. When $G$=100 K·mm$^{-1}$, no equiaxed crystals are observed and the growth velocity of the columnar crystals increases with an increase in $V_{\mathrm{c}}$. When $G$=40 K·mm$^{-1}$, the CET phenomenon appears only at $V_{\mathrm{c}}$=2.4 K·s$^{-1}$. When $G$ decreases to 10 K·mm$^{-1}$, a clear crystal transition phenomenon is observed. With the increase of solidification velocity, the columnar crystal zone is shrinking and the number of equiaxial crystals is getting more and more, but the columnar crystals will not completely disappear even when $V_{\mathrm{c}}$=2.4 K·s$^{-1}$. Under this condition, the length of columnar crystals is primarily controlled by $V_{\mathrm{c}}$ and is inversely proportional to $V_{\mathrm{c}}$. When $G$ reaches 4 K·mm$^{-1}$, a similar phenomenon is observed, but at a high cooling rate, all columnar crystals become isometric. Such a pattern has been found in many experimental and simulation studies[10, 23, 42, 44]. Keeping $G$ at 1 K·mm$^{-1}$, the nucleation density is lower and the dendrite size is larger when $V_{\mathrm{c}}$ is lower. This is due to the fact that the solutes released during the growth of dendrites inhibit the nucleation of the grains, and there is more space for dendrites to grow, therefore, the size of the dendrites in the remaining liquid is significantly larger[45].

### 4.2.1 Effect of solidification parameters on equiaxed crystals

As can be seen in Fig. 6, the dendrites can be divided into three regions based on their morphology: an equiaxial crystallization region, a CET region, and a columnar crystallization region, with variations in $G$ and $V_{\mathrm{c}}$. In the equiaxed crystal region, the effects of $G$ and $V_{\mathrm{c}}$ on dendrite tip growth rate and solid volume fraction were studied, and the results are shown in Fig. 7(a). Taking $G$=3 K·mm$^{-1}$ as an example, the tip growth rate rapidly increases with an increase in $V_{\mathrm{c}}$ until it reaches 225 μm·s$^{-1}$. The increase in $V_{\mathrm{c}}$ leads to greater undercooling of the dendritic front. This provides the primary driving force for dendritic growth, thereby accelerating the growth rate at the dendrite tip. When $V_{\mathrm{c}}$ remains constant, an increase in $G$ leads to a larger free energy difference. This provides a greater driving force, accelerating the growth at the dendrite tip.

With the $G$ maintains at $G$=1 K·mm$^{-1}$, the effect of $V_{\mathrm{c}}$ on the

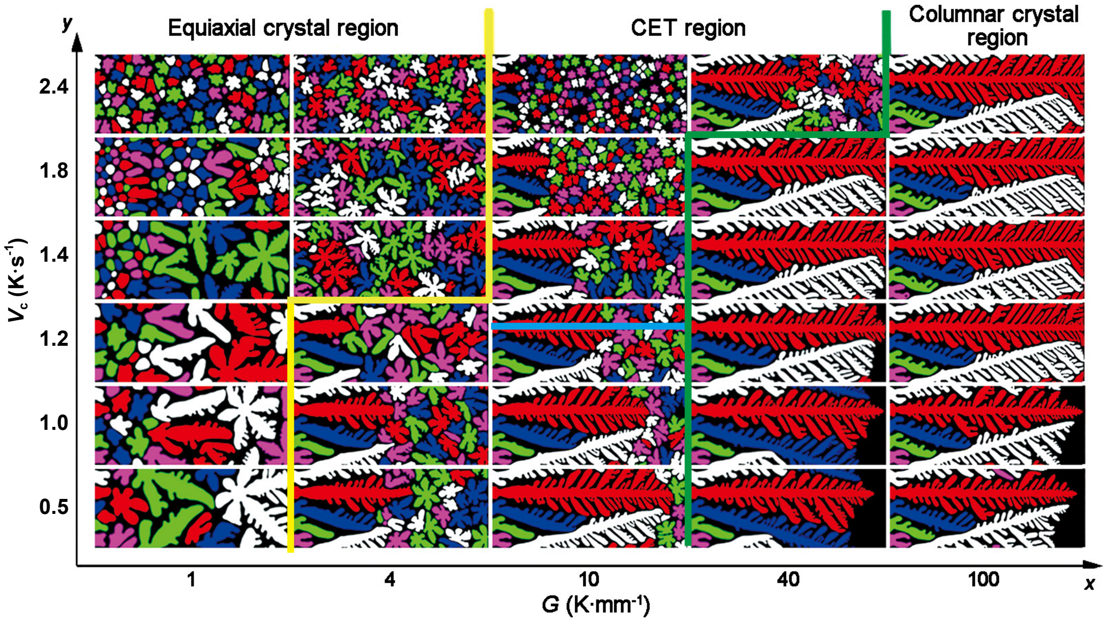

**Fig. 6: Simulation results of dendrite morphology under different solidification conditions**

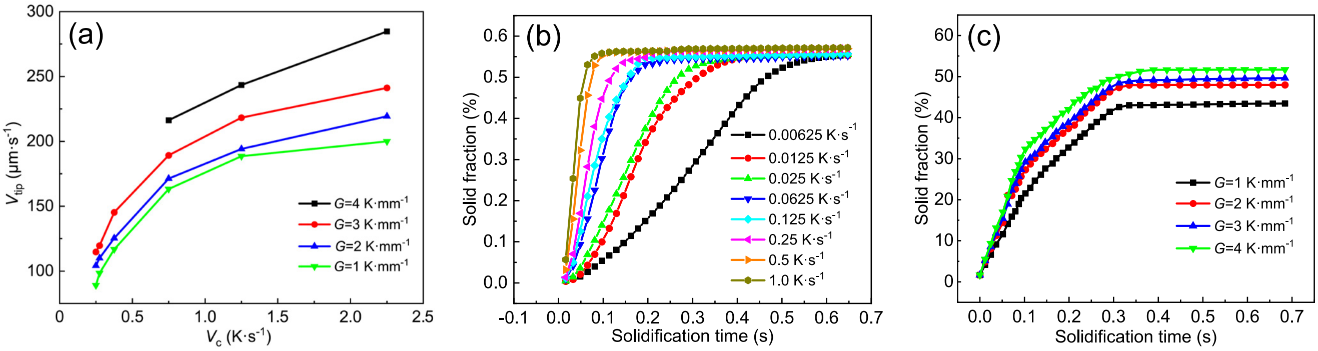

**Fig. 7: Effect of cooling rate ($V_c$) and temperature gradient ($G$) on dendrite tip growth rate ($V_{tip}$) and solid phase volume fraction in equiaxed crystal region: (a) $V_{tip}$ varying with $V_c$ and $G$; (b) solid phase volume fraction varying with $V_c$ under $G$=1 K·mm$^{-1}$; and (c) solid phase volume fraction varying with $G$ under $V_c$=1.4 K·s$^{-1}$**

solid phase volume fraction was investigated. As shown in Fig. 7(b), in the early stage of solidification, the solid phase volume fraction sharply increases with an increase in $V_c$, but gradually stabilizes in the late stage of solidification. As $V_c$ increases, the subcooling degree increases. This leads to an increase in the number of active nuclei, which in turn increases the solid phase volume fraction. At late solidification stage, the solid fraction tends to be steady because the undercooled melt is almost exhausted.

When the $V_c$ maintains at $V_c$=1.4 K·s$^{-1}$, the effect of $G$ on the solid phase volume fraction was investigated. As shown in Fig. 7(c), a similar trend of variation is observed: the solid phase volume fraction rapidly increases with an increase in $G$ in the early stage of solidification and then gradually stabilizes in the late stage of solidification. With the increase of $G$, the number of active nuclei increases. This in turn leads to an increase in the solid phase volume fraction.

### 4.2.2 Effect of solidification parameters on solute change pattern in CET transition

As shown in Fig. 6, with in the CET transition region, a larger $V_c$ leads to an earlier onset of dendritic transition; whereas a higher $G$ results in a delayed onset of dendritic transition. This is because both $V_c$ and $G$ affect the solute distribution in the dendrite, which in turn has an effect on the crystalline transition. Therefore, to deeply analyze the solute changes during the CET process, the dendritic morphology corresponding to a cooling rate $V_c$ of 1.2 K·s$^{-1}$ and a temperature gradient $G$ of 10 K·mm$^{-1}$ was selected for detailed investigation, as shown in Fig. 8. A detailed analysis of the variation of Gd element concentration ($c$) along the blue axis in Fig. 8 was performed, and the results are shown in Fig. 9.

**Fig. 8: Simulation results of dendrite morphology with $V_c$=1.2 K·s$^{-1}$ and $G$=10 K·mm$^{-1}$**

The area enclosed by the red ellipse in Fig. 9(a1) represents the equiaxed crystal region, while the other region represents the columnar crystal region. The peaks and troughs correspond to the interdendritic regions and the dendrite interiors, respectively. Based on the illustration, it can be observed that different regions exhibit different solute concentrations. Specifically, the interiors of the dendrites have lower solute concentrations, while the interdendritic regions show higher solute concentrations. This is due to the fact that the rate of solute discharge within the dendrites is higher than the rate of solute diffusion in the interdendrite regions. As a result, the solute cannot diffuse away efficiently, leading to its accumulation primarily in the interdendritic regions. Therefore, the solute concentration in the dendritic region is relatively high. Additionally, when $G$=40 K·mm$^{-1}$, as shown in Figs. 9(c1–c3), the dendrites are entirely columnar crystals, and the solute concentration in the interdendritic regions decreases with an increase in $V_c$. This is because, in this case, the influence of equiaxed crystals is absent, and the growth of columnar crystals is not inhibited. As a result, a relatively large solute diffusion zone forms at the dendrite tip. As solidification progresses, the solute at the tip undergoes sufficient diffusion, thus leading to a relatively lower concentration at the tip of the dendrite.

It can be seen that a decrease in $G$ leads to an increase in the number of equiaxed grains when $V_c$ is constant. This is due to the fact that the lower the $G$, the greater the initial subcooling. As a result, the growth of dendrites is accelerated and the number of equiaxed grains increases. Similarly, the number of equiaxed grains increases with an increase in $V_c$, because increasing $V_c$ also results in the increase of initial subcooling.

The graph also shows that when the cooling rate maintains constant, a decrease in temperature gradient leads to a gradually decrease in the length of the columnar crystal region. In the same way, when the temperature gradient remains constant, an increase in the cooling rate leads to a gradual reduction in the length of the columnar crystal region. This suggests that lowering the temperature gradient or increasing the cooling rate not only promotes the growth of equiaxed grains, but also inhibits the growth of columnar crystals. Therefore, it can be concluded that the transformation of crystal morphology is primarily controlled by the temperature gradient and cooling rate. Specifically, a higher cooling rate results in the earlier appearance of this transition. The main reason is that both increasing the cooling rate and decreasing the temperature gradient can increase the initial subcooling. The greater the subcooling, the greater the driving force for dendrite growth and therefore the faster the dendrite growth. This results in equiaxed grains starting to appear before the columnar crystals are fully developed. This is similar to the observations of Sturz et al[12].

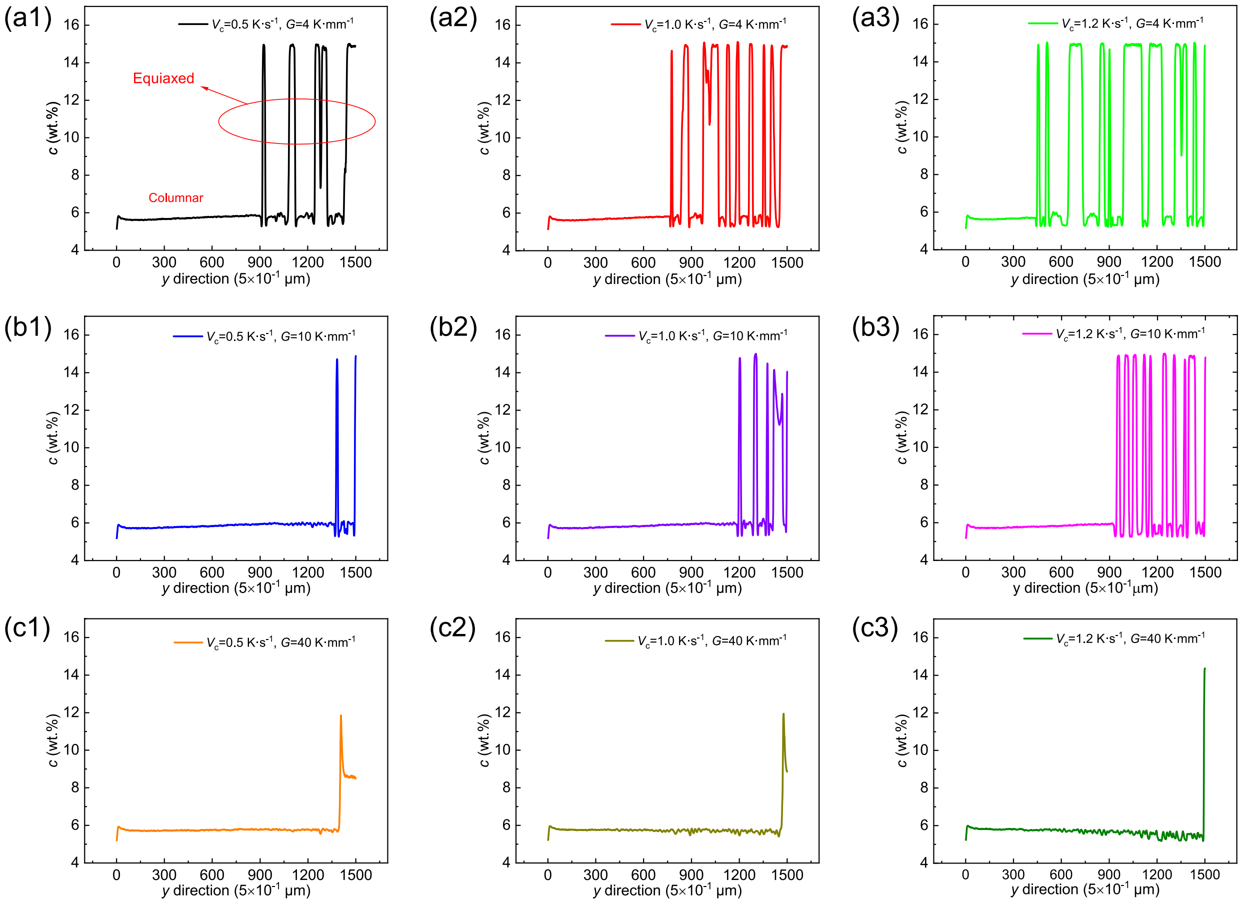

**Fig. 9: Variation of Gd elemental concentration on the central axis of the red columnar crystal (bule line in Fig. 8) at different cooling rates and temperature gradients in the crystal transition region: (a1–a3) $G$=4 K·mm$^{-1}$; (b1–b3) $G$=10 K·mm$^{-1}$; (c1–c3) $G$=40 K·mm$^{-1}$**

### 4.2.3 Effect of solidification parameters on columnar crystal

In order to deeply analyze the role of solidification parameters, the effect of cooling rates and temperature gradients on the growth of columnar crystals, separately, was investigated, and the results are shown in Fig. 10. When $G$=1 K·mm$^{-1}$, the length of columnar crystals increases with the increase of $V_c$ [Fig. 10(a)]. When keeping $V_c$=1.25 K·s$^{-1}$, the increase of $G$ promotes the growth of columnar crystals [Fig. 10(b)]. This is due to an increase in the cooling rate and temperature gradient resulting in an increase in subcooling. The increase in supercooling provides a stronger driving force that promotes the growth rate of dendrites and ultimately increases the length of columnar crystals.

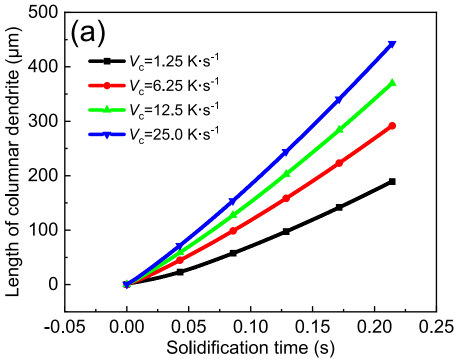

**Fig. 10: Effect of cooling rate, as $G$=1 K·mm$^{-1}$ (a) and temperature gradient, as $V_c$=1.25 K·s$^{-1}$ (b) on the length of columnar crystals**

The primary dendrite arm spacing (PDAS) is one of the important parameters affecting the alloy properties, such as fatigue strength and creep resistance[44, 46]. There are many studies on PDAS, and the more mature ones are Nastac model[47], Huang model[48], Kurz-Fisher[39] model, and Trivedi model[42]. The Nastac model estimated the dendrite arm spacing through differential thermal analysis (DTA). The Huang model, Kurz-Fisher model, and Trivedi model further explained the change of PDAS ($\lambda_1$) and growth rate ($V_{\mathrm{P}}$).

The Nastac model is:

$$\lambda_1 = \mu_{\mathrm{PDAS}} V_{\mathrm{P}}^{-1/4} G^{-1/2} \tag{16}$$

where $\mu_{\mathrm{PDAS}}$ is a constant.

Huang found the following relationship:

$$\lambda_1 = aV\mathrm{c}^{-b} \tag{17}$$

where $a$ and $b$ are constants related to the materials.

The Kurz-Fisher model is:

$$\lambda_1 = 4.3\Delta T_{\mathrm{n}}^{0.5}\left(\frac{D_1\gamma}{\Delta T_0 k}\right)^{0.25} G^{-0.5} V_{\mathrm{P}}^{-0.25} \tag{18}$$

where $\Delta T_{\mathrm{n}}$ is the nucleation undercooling of the Mg-Gd-Zn alloys, and $\Delta T_0$ is the temperature range of the equilibrium solidification.

The Trivedi model is:

$$\lambda_1 = 2.83(L\Delta T_0 k D_1 \gamma)^{0.25} G^{-0.5} V_{\mathrm{P}}^{-0.25} \tag{19}$$

where $L$ is the harmonic disturbance coefficient.

The simulations using the phase-field method and compared the results with the Nastac, Huang, Kurz-Fisher, and Trivedi models were performed, and the results are shown in Fig. 11. Both the phase-field simulation and the other models show the same trend, i.e., the PDAS decreases as $V_c$ increases. This is because increasing the cooling rate will increase the degree of subcooling, thereby enhancing the nucleation rate of the crystals and thus leading to an increase in the number of columnar crystals. As the number of columnar crystals increases, the growth space of the dendrites becomes limited, leading to a reduction in the spacing between primary dendrite arms. And yet, there are differences between the models. As can be seen from Fig. 11, the phase-field simulation results are closer to the Nastac model, but there is a large deviation between them and the Trivedi model. This discrepancy is mainly due to the fact that the scaling constants of the Trivedi model are estimated based on aluminum alloys.

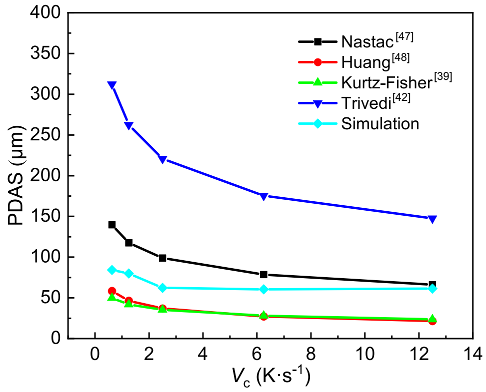

**Fig. 11: Variation of PDAS with different cooling rates**

### 4.2.4 Construction of crystallographic transition diagrams

Crystallographic transition diagrams are important guides in our experiment. Therefore, phase field simulations were used to create a crystallographic transition map. While, the prerequisite for establishing the crystalline transition map is the accurate prediction of the CET transition under different cooling rate and temperature gradient conditions. In recent years, many researchers have developed various CET prediction models. One of the most common models is the GTK model proposed by Gäumann et al[14]. The GTK model is mainly used to study the effects of nucleation subcooling, nucleation density, and solute content on crystal transformation. The model expression is as follows:

$$\frac{\Delta T_{\mathrm{n}}}{V_{\mathrm{p}}}=\alpha\left[\sqrt[3]{\frac{-4\pi N_0}{3\ln(1-f)}}\times\frac{1}{n+1}\right]^n \tag{20}$$

where $\alpha$ and $n$ are the material-related coefficients, $N_0$ is the nucleation rate, and $f$ is the volume fraction of the equiaxed crystal.

Simulations using the phase-field method was conducted to statistically analyze the dendritic morphology under different cooling rates and temperature gradients in this work. As shown in Fig. 12, the individual crystalline regions can be obtained. In the GTK model, if the volume fraction of the equiaxed crystals is less than 0.0066, the crystal transition does not occur, and the dendrites are all columnar crystals. When the volume fraction of the equiaxed grains is greater than 0.49, all grains exist in the form of equiaxed grains. When comparing the simulation results with the GTK model results, it can be found that the phase-field method yields consistent results with the predictions of the GTK model. Therefore, the present model with the proposed nucleation model can reasonably predict different solidification regimes.

## 4.3 Effect of nucleation on crystal transition

Critical undercooling and nucleation density influence nucleation processes, which are crucial factors in crystal transformation. Therefore, this study investigated the effects of critical undercooling and nucleation density on crystal transformation.

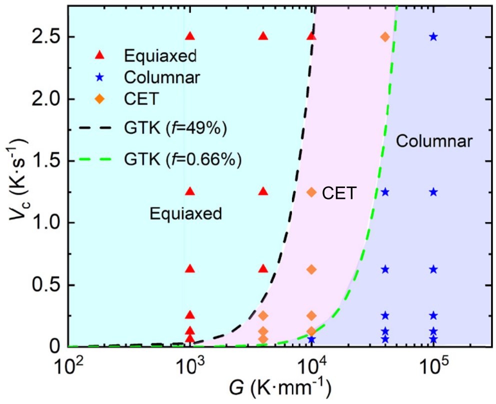

**Fig. 12: Prediction results of CET region**

### 4.3.1 Effect of critical nucleation undercooling on crystal transition

Critical undercooling can determine the intermediate axial nucleation in the front of columnar crystals[49]. Nucleation is possible only when the liquid undercooling is greater or equal to the critical nucleation undercooling. Figure 13 shows the simulation results of the CET under different critical nucleation undercooling degrees when $G$=40 K·mm$^{-1}$ and $V_{\mathrm{p}}$=250 μm·s$^{-1}$. When the critical nucleation undercooling is 4 K, a large number of equiaxed crystals begin to nucleate in the front of columnar crystals in Fig. 13(a). When the critical undercooling increases to 8 K, the equiaxed crystals disappear and the solidification structure is mostly composed of columnar crystals.

The relationship between critical nucleation undercooling and the number of grain nucleation is shown as[12]:

$$\ln(N)=\ln B-a\Delta T_{\mathrm{n}}^{-1} \tag{21}$$

where $a=\dfrac{4\gamma_{\mathrm{SL}}}{\Delta S_{\mathrm{V}}d_0}$, $\gamma_{\mathrm{SL}}$ represents the interfacial energy at the solid-liquid interface, $\Delta S_{\mathrm{V}}$ is the entropy of melting per unit volume, $d_0$ represents the characteristic diameter of the size distribution, and $B$ is a constant.

Figure 14 shows the relationship between the nucleation number and the critical nucleation undercooling. The data for the nucleation undercooling between 4–6 K conform to the relationship indicated by Eq. (21), i.e., $a$=–8.352 and ln$B$=1.614. However, the data deviation at nucleation undercooling of 6.5 K is relatively large. The main reason may be the sudden increase of nucleation undercooling, which raises the required nucleation energy for grains. As a result, the conditions necessary to satisfy Eq. (21) are no longer met.

To study the concentration distribution under different critical nucleation subcooling conditions, the same location was analyzed, as shown in Fig. 3, which is randomly selected and indicated by the solid yellow line. As shown in Fig. 15, the concentration curve fluctuates drastically in the equiaxed crystal region when the critical nucleation undercooling is 4 K in Fig. 15(a), indicating that there are more nucleated grains in the front of columnar crystals. With the increase of the critical nucleation undercooling, the concentration curve becomes gentle, and the length of columnar crystal increases [see Figs. 15(b–e)].

**Fig. 13: Simulation results of CET under different critical nucleation undercooling degrees with $G$=40 K·mm$^{-1}$ and $V_{\mathrm{P}}$=250 μm·s$^{-1}$: (a) $\Delta T_{\mathrm{n}}$=4 K; (b) $\Delta T_{\mathrm{n}}$=4.5 K; (c) $\Delta T_{\mathrm{n}}$=5.5 K; (d) $\Delta T_{\mathrm{n}}$=6 K; (e) $\Delta T_{\mathrm{n}}$=6.5 K; (f) $\Delta T_{\mathrm{n}}$=8 K**

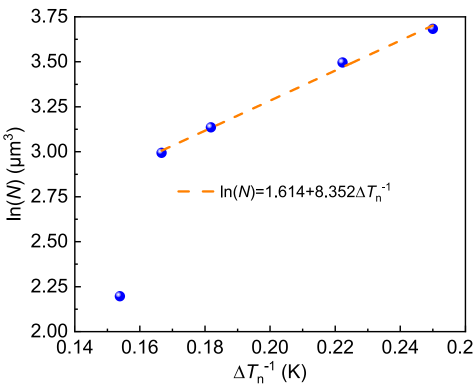

**Fig. 14: Relationship between the number of nucleation (*N*) and the critical nucleation undercooling ($\Delta T_n$) in Mg-15Gd-Zn (wt.%) alloy**

When the undercooling reaches 8 K [Fig. 15(f)], the fluctuation of the concentration curve disappears, but the fluctuation of concentration inside the columnar crystals becomes more serious. The reason may be that an increase in the critical nucleation undercooling is unfavorable for dendrite nucleation, while the growth of columnar crystals remains unaffected and proceeds at a relatively fast rate. This results in solute enrichment between the secondary dendritic arms, leading to fluctuations in the concentration profiles.

### 4.3.2 Effect of nucleation density on crystal transition

The nucleation density is related to the nuclei number. The dendrite nucleation energy can be reduced by adding nucleating agents, which increases the number of dendrite nucleation.

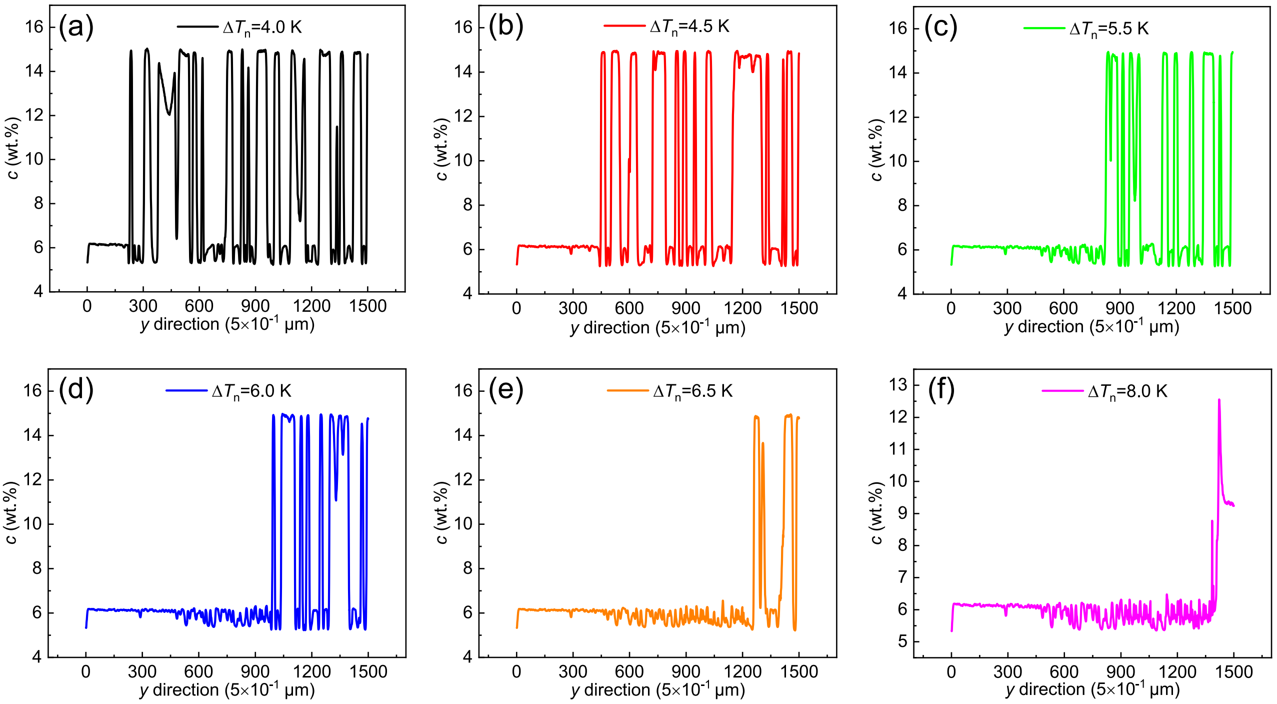

**Fig. 15: Concentration distribution along the yellow solid line in Fig. 13**

The variation of nucleation density from 0 to 5.0 mm$^{-2}$ for $G$=4 K·mm$^{-1}$ and $V_c$=1.8 K·s$^{-1}$ were investigated, and the results are shown in Fig. 16. When the nucleation density is 0 mm$^{-2}$ in Fig. 16(a), no equiaxed crystal is formed at the tip of the dendrite. When the nucleation density is 0.2 mm$^{-2}$ and 0.5 mm$^{-2}$ [Figs. 16(b) and (c)], only a few equiaxed crystals are formed at the tip of dendrites. The dendrites are relatively coarse, and the growth of columnar crystals is not completely inhibited. When the nucleation density is increased to 1.0 mm$^{-2}$ and 2.0 mm$^{-2}$, the nucleation of equiaxed crystal is promoted ahead of the columnar crystals [Figs. 16(d) and (e)]. Further increasing the nucleation density to 5.0 mm$^{-2}$ [Fig. 16(f)], a number of equiaxed crystals nucleate in the liquid phase, resulting in finer grain size, indicating that increasing the nucleation density can promote the occurrence of CET.

The influence of nucleation density on CET position and equiaxed crystal grain diameter are shown in Fig. 17. Both the CET location and dendrite diameter decrease with an increase in nucleation density. When the nucleation density is low, the number of equiaxed crystals nucleated ahead of columnar crystals is small, and the spacing between equiaxed crystals is large. At this time, the competition between dendrites is weak, which is conducive to the growth of columnar crystals. With an increase in nucleation density, the number of equiaxed crystals increases, which reduces the available growth space for columnar crystals and inhibits their full development.

## 5 Conclusions

(1) As the cooling rate increases, the number of nuclei rises and the grain size decreases. Likewise, increasing the cooling rate leads to reductions in the dendrite tip radius and secondary dendrite arm spacing. Simulation outcomes show good quantitative agreement with experimental measurements across a range of solidification conditions.

(2) In the equiaxed region, as the temperature gradient and

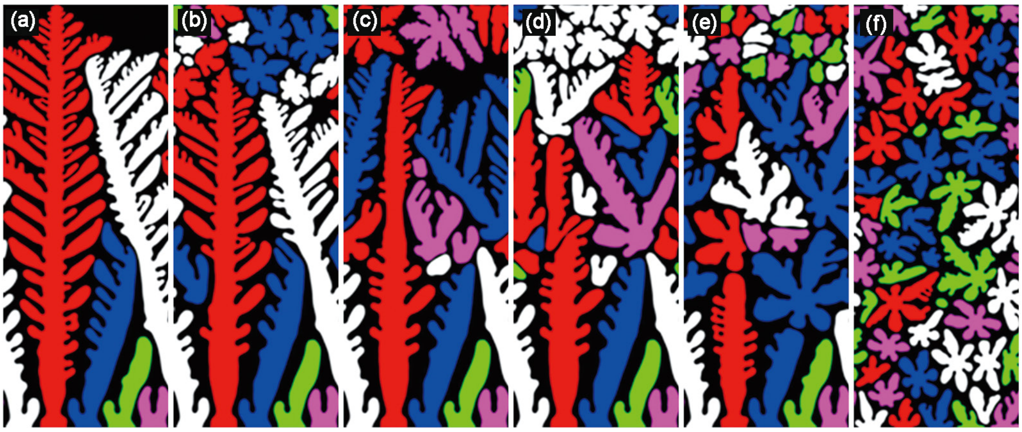

**Fig. 16: Effect of nucleation density on CET under $G$=4 K·mm$^{-1}$ and $V_c$=1.8 K·s$^{-1}$: (a) $N$=0 mm$^{-2}$; (b) $N$=0.2 mm$^{-2}$; (c) $N$=0.5 mm$^{-2}$; (d) $N$=1.0 mm$^{-2}$; (e) $N$=2.0 mm$^{-2}$; (f) $N$=5.0 mm$^{-2}$**

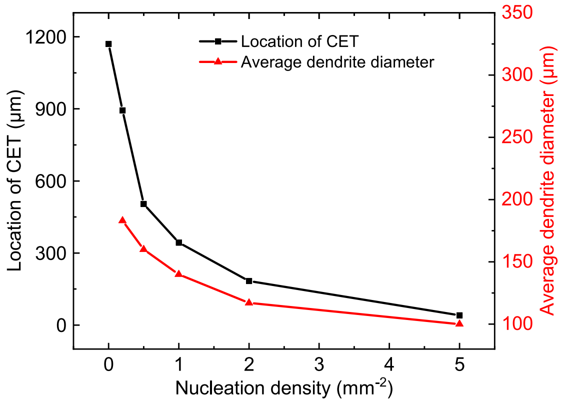

**Fig. 17: Influence of nucleation density on CET position and mean dendrite diameter**

cooling rate increase, both the tip growth rate and solid phase volume fraction increase. In the CET region, decreasing the temperature gradient and increasing the cooling rate are both favorable for the CET process. In the columnar region, increasing the cooling rate decreases the primary dendrite arm spacing.

(3) As the critical nucleation undercooling increases, the equiaxed crystals ahead of the columnar grain interface disappear, and the columnar crystal region continues expanding. The relationship between the critical nucleation undercooling $\Delta T_n$ and the grain nucleation number $N$ is expressed as $\ln(N)$=1.614+8.352$\Delta T_n^{-1}$, i.e. $\Delta T_n$ is proportional to $N$. With an increase in nucleation density, the nucleation of equiaxed crystals ahead of the columnar crystal interface is promoted, which inhibits the growth of columnar crystals.

## Acknowledgments

This work was financially supported by the Postdoctoral Research Project of Henan Province (No. 202101003), the Key Research Programs of Higher Education Institutions in Henan Province (Nos. 24A450003, 23A460016), the Henan Provincial Key Laboratory of Intelligent Manufacturing of Machinery and Equipment Open Subjects (No. IM202308), the Zhengzhou University of Light Industry Doctoral Research Initiation Fund (No. 2019BSJJ005), and the Henan Provincial Science and Technology Tackling Project (No. 23A460016).

## Conflict of interest

The authors have no competing interests to declare that are relevant to the content of this article.

## References

[1] Peng D H, Li F, Wang Y, et al. Annealing coordinates the deformation of shear band to improve the microstructure difference and simultaneously promote the strength-plasticity of composite plate. Materials & Design, 2022, 219: 110696.

[2] Michiaki Y, Shi Z M, Andrej A, et al. Influence of crystallographic orientation and Al alloying on the corrosion behaviour of extruded α-Mg/LPSO two-phase Mg-Zn-Y alloys with multimodal microstructure. Corrosion Science, 2022, 200: 110237.

[3] Xi G Q, Zhao X H, Ma Y L, et al. Comparative study on corrosion behavior and mechanism of as-cast Mg-Zn-Y and Mg-Zn-Gd alloys. Acta Metallurgica Sinica, 2023, 36(2): 310–322.

[4] Meng S J, Yu H, Fan S D, et al. Recent progress and development in extrusion of rare earth free Mg alloys: A review. Acta Metallurgica Sinica, 2019, 32(2): 145–168.

[5] Constantin B, Christian H, Jonas W, et al. Analytical description of the criterion for the columnar-to-equiaxed transition during laser beam welding of aluminum alloys. Metallurgical and Materials Transactions: A, 2021, 52(7): 2720–2731.

[6] Gao Z G. Numerical analysis of stray grain formation during laser welding nickel-based single-crystal superalloy, Part I: Columnar/equiaxed morphology transition. Journal of Physics: Conference Series. IOP Publishing, 2021, 1888(1): 012004.

[7] Xu X S, Ding H S, Huang H T, et al. Microstructure formation and columnar to equiaxed transition during cold crucible directional solidification of a high-Nb TiAl alloy. Journal of Materials Research and Technology, 2021, 11: 2221–2234.

[8] Wajira U M, Dai H J, Dong H B, et al. Computational modeling of columnar to equiaxed transition in alloy solidification. Advanced Engineering Materials, 2013, 15(4): 216–229.

[9] László G, Gyula I T, James A W, et al. Phase-field modeling of crystal nucleation in undercooled liquids: A review. Progress in Materials Science, 2019, 106: 100569.

[10] Wang Y B, Jia S S, Wei M G, et al. Research progress on solidification structure of alloys by synchrotron X-ray radiography: A review. Journal of Magnesium and Alloys, 2020, 8: 396–413.

[11] Hunt J D. Steady state columnar and equiaxed growth of dendrites and eutectic. Materials Science and Engineering, 1984, 65(1): 75–83.

[12] Sturz L, Drevermann A, Pickmann C, et al. Influence of grain refinement on the columnar-to-equiaxed transition in binary Al alloys. Materials Science and Engineering: A, 2005, 413: 379–383.

[13] Zaïdat K, Ouled-Khachroum T, Mangelinck-Noël N, et al. Effect of travelling magnetic field on the directional solidification of refined Al-3.5 wt%Ni alloys. Materials Science Forum, 2006, 508: 221–226.

[14] Gäumann M, Trivedi R, Kurz W. Nucleation ahead of the advancing interface in directional solidification. Materials Science and Engineering: A, 1997, 226: 763–769.

[15] Gäumann M, Henry S, Cléton F, et al. Epitaxial laser metal forming: Analysis of microstructure formation. Materials Science and Engineering: A, 1999, 271(1–2): 232–241.

[16] Mathiesen R H, Arnberg L. X-ray radiography observations of columnar dendritic growth and constitutional undercooling in an Al-30wt%Cu alloy. Acta Materialia, 2005, 53(4): 947–956.

[17] Kang M D, Gao H Y, Shu D, et al. In situ and real-time observation of the solidification process of Al-20 mass% Cu alloy by synchrotron X-ray radiography. Materials Transactions, 2014, 55(5): 774–778.

[18] Garces G, Medina J, Perez P, et al. The effect of temperature on load partitioning evolution in magnesium metal matrix composite reinforced with Ti particles using in-situ synchrotron radiation diffraction experiments. Journal of Magnesium and Alloys, 2022, 11(2): 23–41.

[19] Xin T Z, Tang S, Ji F, et al. Phase transformations in an ultralight BCC Mg alloy during anisothermal ageing. Acta Materialia, 2022, 239: 118248.

[20] Badillo A, Beckermann C. Phase-field simulation of the columnar-to-equiaxed transition in alloy solidification. Acta Materialia, 2006, 54(8): 2015–2026.

[21] Li J J, Wang J C, Yang G C. Phase-field simulation of microstructure development involving nucleation and crystallographic orientations in alloy solidification. Journal of Crystal Growth, 2007, 309(1): 65–69.

[22] Viardin A, Sturz L, Zimmermann G, et al. Phase-field modeling of the columnar-to-equiaxed transition in neopentylglycol-camphor alloy solidification. Journal of Physics: Conference Series, 2011, 327: 012004.

[23] Rátkai L, Tóth G I, Környei L, et al. Phase-field modeling of eutectic structures on the nanoscale: the effect of anisotropy. Journal of Materials Science, 2017, 52(10): 5544–5558.

[24] Lenart R, Eshraghi M. Modeling columnar to equiaxed transition in directional solidification of Inconel 718 alloy. Computational Materials Science, 2019, 172: 109374.

[25] Montiel D, Liu L, Xiao L, et al. Microstructure analysis of AZ31 magnesium alloy welds using phase-field models. Acta Materialia, 2012, 60(16): 5925–5932.

[26] Raghavan N, Dehoff R, Pannala S, et al. Numerical modeling of heat-transfer and the influence of process parameters on tailoring the grain morphology of IN718 in electron beam additive manufacturing. Acta Materialia, 2016, 112: 303–314.

[27] Nabavizadeh S A, Eshraghi M, Felicelli S D. Three-dimensional phase field modeling of columnar to equiaxed transition in directional solidification of Inconel 718 alloy. Journal of Crystal Growth, 2020, 569: 125879.

[28] Wang Y B, Peng L M, Ji Y Z, et al. Effect of cooling rates on the dendritic morphology transition of Mg-6Gd alloy by in situ X-ray radiography. Journal of Materials Science & Technology, 2018, 34(7): 1142–1148.

[29] Wang Y B, Jia S S, Wang M Y, et al. Coupling in situ synchrotron X-ray radiography and phase-field simulation to study the effect of low cooling rates on dendrite morphology during directional solidification in Mg-Gd alloys. Journal of Alloys and Compounds, 2020, 815: 152385.

[30] Liu X T, Sun Y Q, Wang Y B, et al. The effect of cross-section geometry of castings on dendrite evolution in MgGd alloys by in situ X-ray radiography. Materials Characterization, 2022, 186: 111751.

[31] Alain K, Wouter-Jan R. Phase-field model of dendritic sidebranching with thermal noise. Physical Review: E, 1999, 60(4): 3614.

[32] Sun D Y, Mendelev M I, Becker C A, et al. Crystal-melt interfacial free energies in hcp metals: A molecular dynamics study of Mg. Physical Review: B, 2006, 73(2): 024116.

[33] Sarreal J A, ABbaschian G J. The effect of solidification rate on microsegregation. Metallurgical Transactions: A, 1986, 17: 2063–2073.

[34] Bryan Z L, Alieninov P, Berglund I S, et al. A diffusion mobility database for magnesium alloy development. Calphad, 2015, 48: 123–130.

[35] Zhou B C, Shang S L, Wang Y, et al. Data set for diffusion coefficients of alloying elements in dilute Mg alloys from first-principles. Data in Brief, 2015, 5(C): 900–912.

[36] Zhou B C, Shang S L, Wang Y, et al. Diffusion coefficients of alloying elements in dilute Mg alloys: A comprehensive first-principles study. Acta Materialia, 2016, 103: 573–586.

[37] Eskin D, Du Q, Ruvalcaba D, et al. Experimental study of structure formation in binary Al-Cu alloys at different cooling rates. Materials Science and Engineering: A, 2005, 405(1–2): 1–10.

[38] Young K P, Kerkwood D H. The dendrite arm spacings of aluminum-copper alloys solidified under steady-state conditions. Metallurgical Transactions: A, 1975, 6(1): 197–205.

[39] Kurz W, Fisher D J. Dendrite growth at the limit of stability: Tip radius and spacing. Acta Metallurgica, 1981, 29(1): 11–20.

[40] Somboonsuk K, Mason J T, Trivedi R. Interdendritic spacing: Part I. Experimental studies. Metallurgical and Materials Transactions: A, 1984, 15: 967–975.

[41] Dominique B, John S K. Prediction of dendrite arm spacings in unsteady- and steady-state heat flow of unidirectionally solidified binary alloys. Metallurgical and Materials Transactions: B, 1997, 28(4): 651–663.

[42] Trivedi R, Somboonsuk K. Constrained dendritic growth and spacing. Materials Science and Engineering: A, 1984, 65(1): 65–74.

[43] Kattamis T Z, Flemings M C. Dendrite structure and grain size of undercooled melts. In: Proc. the Merton C. Flemings Symposium on Solidification and Materials Processing, 2000: 43–52.

[44] Tourret D, Karma A. Growth competition of columnar dendritic grains: A phase-field study. Acta Materialia, 2015, 82: 64–83.

[45] Zhao Y, Pu Z, Wang L, et al. Modeling of grain refinement and nucleation behavior of Mg-4Y-0.5Zr (wt.%) alloy via cellular automaton model. International Journal of Metalcasting, 2022, 16: 945–961.

[46] Wilson B C, Cutler E R, Fuchs G E. Effect of solidification parameters on the microstructures and properties of CMSX-10. Materials Science and Engineering: A, 2008, 479(1–2): 356–364.

[47] Nastac L, Valencia J J, Tims M L, et al. Advances in the solidification of IN718 and RS5 alloys. Superalloys, 2001, 718: 625–706.

[48] Huang W D, Geng X G, Zhou Y H. Primary spacing selection of constrained dendritic growth. Journal of Crystal Growth, 1993, 134(1–2): 105–115.

[49] Trivedi R. Interdendritic spacing: Part II. A comparison of theory and experiment. Metallurgical and Materials Transactions: A, 1984, 15(6): 977–982.